High-resolution simulation of the boreal summer intra-seasonal oscillation in Met Office unified model

RMetS
Royal Meteorological Society

High-resolution simulation of the boreal summer intraseasonal oscillation in Met Office Unified Model

Yongjie Fang,[a] Peili Wu,[b]* M. S. Mizielinski,[b] M. J. Roberts,[b] Tongwen Wu,[a] Bo Li,[c] Pier Luigi Vidale,[d] Marie-Estelle Demory[d] and Reinhard Schiemann[d]

[a]*Beijing Climate Center, China Meteorological Administration, Beijing, China*
[b]*Met Office Hadley Centre, Exeter, UK*
[c]*Key Laboratory of Radiometric Calibration and Validation for Environmental Satellites, China Meteorological Administration, Beijing, China*
[d]*National Centre for Atmospheric Science (NCAS-Climate), University of Reading, UK*

*Correspondence to: P. Wu, Met Office Hadley Centre, Fitzroy Rd., Exeter, EX1 3PB, UK. E-mail: peili.wu@metoffice.gov.uk

The present study investigates the fidelity and resolution sensitivity of Met Office Unified Model Global Atmosphere 3.0 in simulating the intraseasonal oscillation (ISO) of the East Asia and western North Pacific summer monsoon. Two sets of model simulations at horizontal resolutions of N216 (60 km) and N96 (130 km) forced by observed daily high-resolution sea-surface temperature are examined and compared with the observations. Diagnostic results show that the model can well reproduce the gross spatio-temporal features of observed summer ISO over East Asia and the western North Pacific in terms of period, dominant rotated empirical orthogonal function (REOF) mode, variance, northward propagation, cycle evolution and vertical structure. The intraseasonal change in intensity and position of the western North Pacific subtropical high and upper troposphere westerly jet associated with the northward propagating ISOs are also reasonably captured in the model. Moreover, increasing horizontal resolution improves most aspects of the ISO simulation, especially the intensity and northward propagation of the ISO-related convection and circulation systems. Further analysis indicates that the improvement as resolution increases is related to the weakening in background state of the East Asian summer monsoon, which is due to the realistic simulation of land–sea thermal contrast in the higher resolution model. This study suggests that enhanced model resolution can have some beneficial impacts on the ISO simulation.

Key Words: intraseasonal oscillation; high resolution modelling; East Asia summer monsoon; Met Office Unified Model

Received 3 February 2016; Revised 30 August 2016; Accepted 12 September 2016; Published online in Wiley Online Library 7 December 2016

1. Introduction

The intraseasonal oscillation (ISO), with periodicity between 10 and 90 days, is a leading mode of intraseasonal variability over the western North Pacific (WNP) and the East Asia region (Yasunari, 1979; Wu, 1993). The boreal summer ISO (BSISO) has a more complex structure compared to the wintertime Madden–Julian Oscillation (MJO: Madden and Julian, 1972), in which eastward propagation dominates, by also exhibiting northward or northwest propagation of convective anomalies (Lau and Chan, 1986; Wu and Li, 1990; Wang and Xie, 1997). The northward propagation of the ISO, characterized by the active and break spells, plays a vital role in the onset and withdrawal of the East Asia and WNP summer monsoon, Meiyu in central China and the Baiu in Japan (Chen and Murakami, 1988; Hsu and Weng, 2001). It also modulates sub-seasonal variability of the subtropical high and tropical cyclone genesis and tracks over the WNP region (Wang and Zhou, 2008; Mao *et al.*, 2010), thus has significant influence on the socio-economic growth of East Asian countries. Considering the crucial role the ISO plays in the East Asia and WNP summer monsoon, improved BSISO simulation in state-of-the-art general-circulation models (GCMs) would have a beneficial impact not only on the extended range prediction of the active and break spells, but also in seasonal prediction.

Simulation of the BSISO over the Asian region has received much attention, but major challenges remain. Typically, model ISOs are too weak and show standing propagation structures (Liu *et al.*, 2008; Kim *et al.*, 2012; Hu *et al.*, 2013). By analysing the ten Atmosphere GCMs (AGCMs) from the monsoon GCMs intercomparison project, Waliser *et al.* (2003) found that most AGCMs fail to represent the eastward propagating convection and the northwest–southeast-tilted rain band associated with

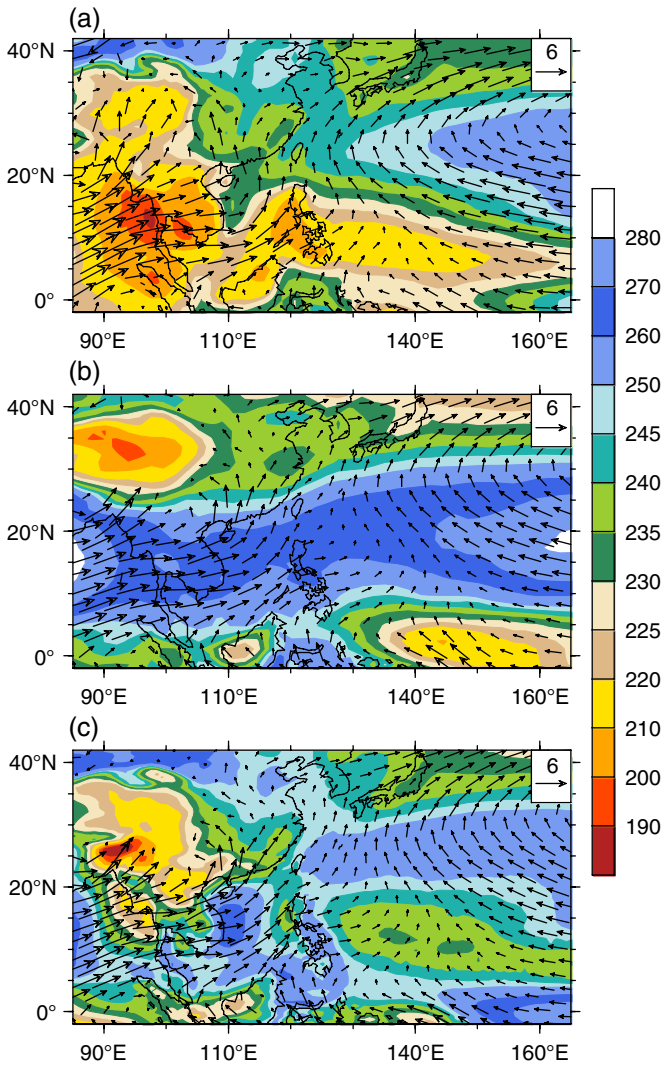

Figure 1. May–September mean OLR (W m^{-2}) and 850 hPa wind vectors from the (a) NOAA and JRA reanalysis, (b) N96, and (c) N216.

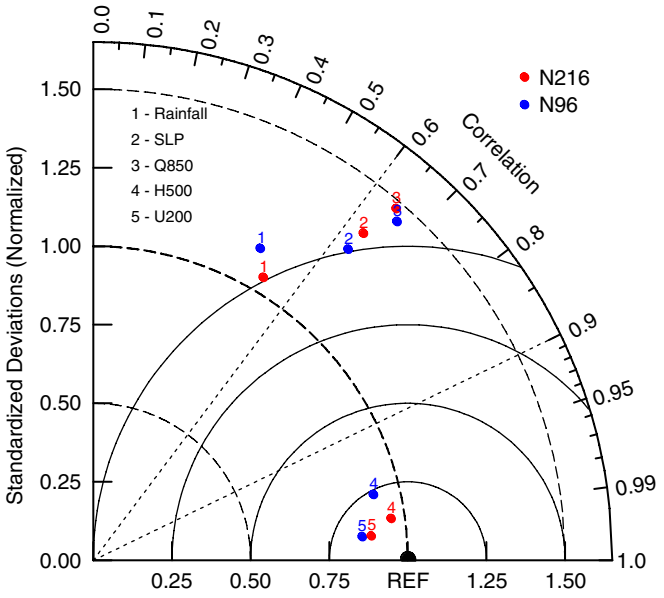

Figure 2. Taylor diagram for GA3.0 at two horizontal resolutions (N96 and N216) to summarize the relative skill to simulate the May–September mean fields over the region (100–150°E, 0–42°N).

the BSISOs, and the model BSISO patterns are typically less coherent and have smaller zonal and meridional spatial scales than the observed patterns. Lin *et al.* (2008) evaluated BSISO over the Asian monsoon region in 14 GCMs and indicated that most of them overestimate the near-equatorial precipitation and underestimate the variability of the northward propagating ISO. ISO in 32 Coupled GCMs (CGCMs) participating in the Coupled Model Intercomparison Project (CMIP) phase 5 was examined by Sabeerali *et al.* (2013). They found that most models could not simulate the spatial pattern of BSISO variance over the Asian monsoon region and fail to simulate the phase relationship between precipitation and wind associated with the northward propagating BSISO.

While the model disagreement in BSISO simulation has been linked to differences in the representation of moisture processes, mean state and air–sea interaction (Fu and Wang, 2004; Ajayamohan and Goswami, 2007; Fang *et al.*, 2013), there are increasing studies concerning the role of the model resolution in representation of ISO/MJO in recent years. These studies indicated that higher resolution models resolving deep convective motions and topography explicitly do not only simulate realistic behaviour of an MJO event (Rajendran *et al.*, 2008; Liu *et al.*, 2009; Satoh *et al.*, 2012), but also realistically capture some aspects of the BSISO in the Indian summer monsoon region (Oouchi *et al.*, 2009; Abhik *et al.*, 2016). As for the East Asia summer monsoon (EASM) region, the resolution sensitivity study of BSISO, however, is less well known. Given the unique characteristics of midlatitude variation and the greater heterogeneity of the underlying surface conditions and topography that the ISO is influenced by, it is necessary to evaluate the performance of high resolution AGCMs in simulating the BSISO over the WNP and East Asia region and to reveal its response to resolution.

In this study, we analyse a series of AMIP-style climate integrations with two different horizontal resolutions of N96 (about 130 km at 50°N) and N216 (about 60 km at 50°N) generated for the United Kingdom on The Partnership for Advanced Computing in Europe (PRACE): weather resolving Simulations of Climate for globAL Environmental risk campaign (UPSCALE campaign: Mizielinski *et al.*, 2014), using the Met Office Unified Model (MetUM) atmosphere–land configuration named Global Atmosphere 3.0 (GA3.0). As many other aspects of the AGCM as possible remain unchanged, which enables investigation into the impact that enhanced resolution has on aspects of East Asia and WNP summer monsoon and its intraseasonal variability, particularly on how the associated processes are better represented. With 27-year (1985–2011) simulations and three ensemble members, this dataset is more extensive than any other individual GCM dataset used to study the resolution sensitivity.

The description of the model, various observational datasets utilized for the evaluation of the simulations and the adopted methodologies are discussed in section 2. Section 3 describes the ability of the model to simulate the mean state of the East Asia and WNP summer monsoon, as well as the temporal and spatial variability of the northward propagating BSISO. The major conclusions and findings of the study are summarized in section 4.

2. The model, data and methodology

2.1. *The Met Office Unified Model*

The climate models used in this study are GA3.0 and Global Land 3.0 (GL 3.0) configurations of the MetUM atmosphere and the Joint UK Land Environment Simulator respectively developed for use in global and regional climate research and weather prediction activities. The default GA3.0 and GL3.0 configurations are documented in Walters *et al.* (2011) and Mizielinski *et al.* (2014). These references describe many relevant developments compared to the Hadley Centre Global Environment Model family version 2 (HadGEM2 Development Team, 2011) from CMIP5, including the standard use of 85 levels up to 85 km for improved stratospheric representation, a prognostic cloud fraction and cloud concentrate scheme (Wilson *et al.*, 2008),

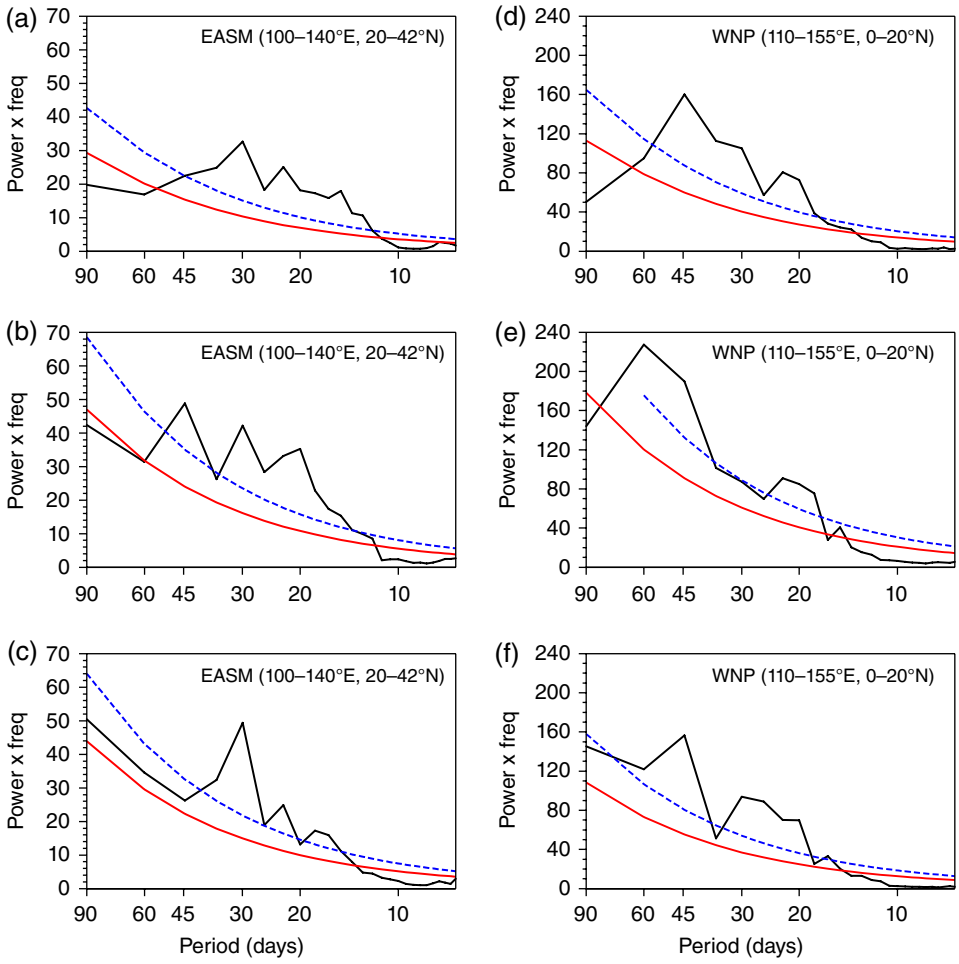

Figure 3. Mean power spectra of OLR for the 15 summers during 1997–2011 over the (a–c) EASM and (d–f) WNP region for (a,d) NOAA reanalysis, (b,e) N96, and (c,f) N216.

modifications to microphysics to reduce the spurious occurrence of drizzle (Abel and Shipway, 2007), and upgraded solar spectrum. A core principle of development of the MetUM is the construction of a traceable hierarchy of model resolutions running from the coarse grids to finer grids. Thus very few scientific settings in the MetUM are changed with resolution, but a few parameters must be changed to ensure numerical stability. These changes include the time step, the magnitude of polar filtering in the advection scheme, and the diffusion of vertical wind velocities in the upper five levels of the atmosphere (Mizielinski *et al.*, 2014). These dynamical adjustments were found not to impact the climatology of the simulations (Demory *et al.*, 2014).

The UPSCALE project (Mizielinski *et al.*, 2014) constructed and ran an ensemble of GA3.0 and GL3.0 global atmosphere-only climate simulations over the period 1985–2011 at different horizontal resolutions, while retaining their vertical resolution. A 15-year period of 1997–2011 is selected from two ensemble integrations at resolution of N96 (130 km) and N216 (60 km) for this study (hereafter referred to as N96 and N216, respectively). The three ensemble members at N216 and five ensemble members at N96, with each member differing only in the initial conditions, follow the Atmospheric Model Intercomparison Project II (AMIP-II) standard but with a few deviations made for scientific reasons. One such deviation is the use of daily sea-surface temperature (SST) and sea ice forcings, derived from the Operational Sea-surface Temperature and sea Ice Analysis (OSTIA) product (Donlon *et al.*, 2012), which has a native resolution of 1/20° and is a synthesis of satellite and *in situ* observations covering 1985 to the present day. OSTIA was chosen because of its finer resolution than other datasets, allowing a richer and more realistic representation of the ocean surface on the model grid. Moreover, the monthly mean value of greenhouse gas and aerosol emissions evolving from 1985 to 2011, defined by the AMIP-II protocols, is imposed in the ensemble simulations.

2.2. *Data and methodology*

The simulations are validated with various observed datasets over the May–September period of 1997–2011. The characteristics of convection in the region are deduced from outgoing long-wave radiation (OLR) data and a merged precipitation analysis. Daily OLR is obtained from the National Oceanic and Atmospheric Administration (NOAA) polar-orbiting satellites (Liebmann and Smith, 1996). Daily precipitation is based on the Global Precipitation Climatology Project (GPCP) rainfall with 1° grid (Adler *et al.*, 2003). The 25-year Japanese Reanalysis (JRA-25: Onogi *et al.*, 2007) daily averaged zonal wind, temperature, geopotential height and specific humidity dataset with 1.25° longitude × 1.25° latitude are utilized to analyse ISO-related variability. Vorticity is computed using u and v wind components from JRA-25 and simulation results.

The Taylor diagram metric (Taylor, 2001) is used to assess the overall performance of the model against observation. To focus on the intraseasonal variability, the daily anomalies for both observations and simulations are calculated by removing the annual cycle, composed of the time mean and the first three harmonics. Then, Lanczos bandpass filters (Duchon, 1979), with 200 weights and retaining periods of 20–70 days, are applied to the anomaly datasets covering all the seasons. Finally, daily anomalies corresponding to the boreal summer season (May–September) are extracted for analysis. Standard metrics, including estimation of variance, power spectra, lag correlation, lag regression, composite analysis, and varimax rotated empirical orthogonal function (REOF) analysis, are applied to evaluate the realism of the simulated BSISO over the East Asia and WNP region.

3. Results

3.1. Mean states

Monsoon ISOs are essentially fluctuations superimposed on the mean monsoon state (Wang and Xie, 1997; Liu and Wang, 2013). We therefore first investigate the simulation of the mean state of the East Asia and WNP summer monsoon. Figure 1 shows the observed and simulated May–September mean OLR and 850 hPa wind field. In observations (Figure 1(a)), a cyclonic low-level circulation associated with the monsoon trough prevails over the South China Sea (SCS), and an expansive anticyclonic circulation, which is part of the Western North Pacific Subtropical High (WNPSH), dominates the WNP region. The WNP summer monsoon corresponds to the band of low outgoing long-wave radiation (OLR) extending from the Pacific intertropical convergence zone westward across the SCS and Indo-China Peninsula. The model at both the horizontal resolutions (Figures 1(b) and (c)) overestimates the OLR to the south of 20°N, especially over the SCS and Indo-China Peninsula, indicating dry bias in these regions. Compared with N96 (Figure 1(b)), N216 (Figure 1(c)) reduces the OLR bias over most of the East Asia and WNP region, especially over the Tibet Plateau and Indo-China Peninsula, probably due to the improved representation of the orography. However, the model shows increasing dry bias over the equatorial western Pacific as resolution increases.

The fidelity of the model to simulate the seasonal mean climatology at two different horizontal resolutions is summarized in the Taylor diagram shown in Figure 2. It assesses the May–September mean spatial pattern correlation, root mean square (RMSE) difference and the simulated to observed ratio of the variances of rainfall, sea-level pressure (SLP), 850 hPa specific humidity (Q850), 500 hPa geopotential (H500), and 200 hPa zonal wind (U200) over the East Asia and WNP region (100–150°E, 0–42°N). The distance from the origin indicates the normalized standard deviation of each variable, while the cosine of the angle swept out by the position vector from the origin indicates the pattern correlation between observed and simulated variable. The distance from the reference point (marked by solid black dot) to the plotted point denotes the RMSE. The isocircles (black concentric circles) of RMSE are drawn based on the skill score calculation using normalized standard deviation and the correlation coefficient. An accurately simulated variable that has least RMSE, highest correlation and normalized standard deviation close to unity should be placed close to the reference point. Figure 2 indicates that the model reasonably produces U200 and H500 over the region, but shows considerably poor skill in simulating the rainfall, Q850 and SLP. Moreover, the close distance between N216 and N96 for all the variables indicates small resolution sensitivity of the seasonal mean state in the model.

3.2. Power spectrum, variance and leading REOF mode

The dominant periodicities of ISO OLR over part of the WNP (110–155°E, 0–20°N) and the EASM region (100–140°E, 20–42°N) were identified through the multi-year mean spectra of 15 summers (May–October) during 1997-2011 (calculated using the unfiltered daily data). Over the EASM region, the observed OLR has a major peak at 30 days, a secondary peak around 20–30 days, and a third peak at 15 days (Figure 3(a)). The N96 captures the 30-day peak, but the 20-day peak is overestimated and there is an additional peak at 45 days (Figure 3(b)). It is noted that N216 captures all the three peaks reasonably, although the variance of the 30-day peak is stronger than the observation (Figure 3(c)). Over the WNP region, the observation has two main peaks at 45 and 20 days respectively (Figure 3(d)). While these two peaks are well reproduced at N216 (Figure 3(f)), an unrealistically strong 60-day peak is produced at N96 (Figure 3(e)). Note also that the observation also has a minor peak around 30 days, which

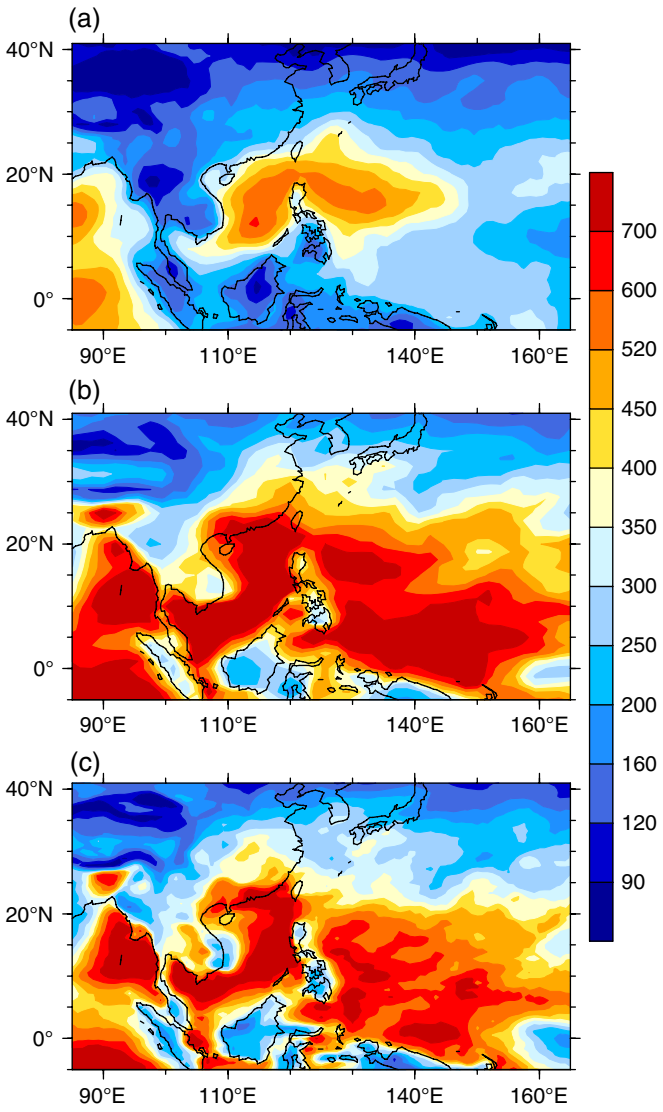

Figure 4. Variance of 20–70-day filtered OLR (W m^{-2}) during the boreal summer (May–September) for (a) NOAA reanalysis, (b) N96, and (c) N216.

is well captured at N216 but absent at N96. Overall, the model captures the dominant periodicities of BSISO over the East Asia and WNP region, and improvements as a result of increased resolution are significant. Given that the dominant periodicity of BSISO over the East Asia and WNP region is 20–70 days, the BSISO signal was extracted from the daily data using a 20–70-day Lanczos filter in the following analyses (Duchon, 1979).

Figure 4 shows the variance of filtered intraseasonal OLR over the WNP region during May–September for the observations, N96 and N216. The intraseasonal variance of observed OLR shows maxima located over the SCS and the Philippine Sea. The N96 captures the above active BSISO centres, but the BSISO variance is overestimated over the whole East Asia and WNP region (Figure 4(b)). When increasing the horizontal resolution to N216, the BSISO variance is significantly reduced, thus comparing better with observation (Figure 4(c)), but the variance is still stronger than the observation. Earlier studies showed that the large-scale horizontal structure of intraseasonal variability and climatological mean state is similar (Liu and Wang, 2013; Shukla, 2014). Therefore, the strong BSISO variance for both the two models is associated with the overestimation of the seasonal mean OLR over the SCS and WNP region as shown in Figure 1.

Lin (2012) and Lee and Wang (2015) extracted the leading modes of the BSISO signals over the East Asia and WNP region using EOF analysis of combined 20–70-day bandpass filtered OLR and 850 hPa zonal winds (U850). They found that the first two leading EOFs reasonably well represent the northward

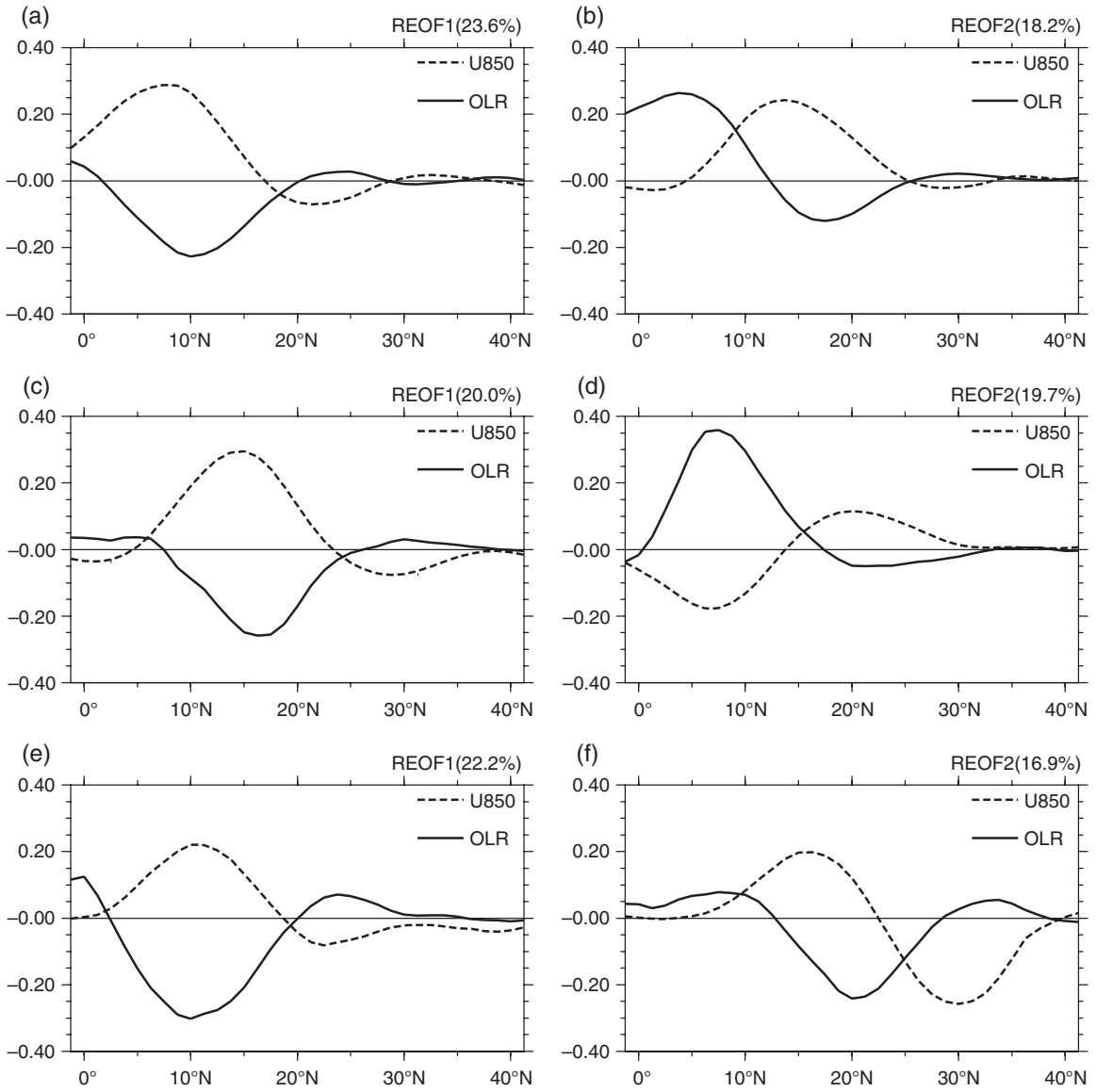

Figure 5. The first (a,c,e) and second (b,d,f) REOF mode of combined analysis of 20–70-day filtered OLR and U850 averaged over 105–145°E during 1997–2011 for (a,b) NOAA and JRA-25 reanalysis, (c,d) N96, and (e,f) N216.

propagation BSISOs. In this study, a REOF, rather than EOF, analysis is performed because it has been demonstrated to be more capable at revealing spatial structures and dividing spatial patterns in comparison studies among the model simulations and observations (Kawamura, 1993).

Analysis here is focused on the first two leading REOF modes of the combined fields of intraseasonal OLR and U850 averaged over 105–145°E, as shown in Figure 5. For the observations, REOF1 is characterized by a negative OLR anomaly with enhanced convection centred near 10°N over the WNP region, whereas EOF2, almost in quadrature to REOF1, has a dipole OLR structure with above-normal convection near 17.5°N (Figures 5(a) and (b)). Additionally, there is a signal displacement of the U850 maxima relative to the convection signal with low-level easterly (westerly) tending to lead (lag) the convective maximum. These two modes are similar to their corresponding EOF modes shown in Lin (2012) and Lee and Wang (2015) despite a 5° southward shift of both the OLR and U850 anomaly centres. Together these two modes constitute the northward propagating BSISOs, and explain more than 40% of the total filtered variance.

The simulated first two leading modes, together accounting for 39.7 and 39.1% of the total explained variance for N96 and N216 respectively, display wind and convection patterns consistent with the observations (Figures 5(c)–(f)). Therefore, the leading REOF pair in the model represent the main structure and northward propagation of the BSISO over the East Asia and WNP region. However, the modelled circulation and convection anomaly centres for both the REOF modes show northward displacement, especially for the N96 simulation (Figures 5(c)–(f)). The BSISO REOF representation for both modes is improved significantly at N216, but the zonal wind anomaly is overestimated over East Asia in REOF2 (Figure 5(f)) and in phase with convection in REOF1 (Figure 5(e)), which is in disagreement with the observation.

3.3. *Northward propagation of BSISO*

To demonstrate the northward propagation and time-varying features of the BSISO over the East Asia and WNP region, lag–latitude correlation and regression analyses were executed. The intraseasonal filtered precipitation averaged over the SCS and Philippine Sea (10–22°N, 110–130°E), where the BSISO has a maximum variance (Figure 4), is used as the reference time series for the correlation and regression. Before being used, the reference time series is standardized by its own standard deviation.

Figure 6 displays the propagation characteristics of 20–70-day filtered precipitation and U850 over the WNP region, constructed from the correlation analysis. Both the two simulations (Figures 6(b) and (c)) capture the observed (Figure 6(a)) northward migration of ISO anomalies over the East Asia and WNP region, with precipitation leading U850 by 3–5 days. The phase relationship is well captured, with westerly anomalies existing under active ISO convection, while an easterly anomaly

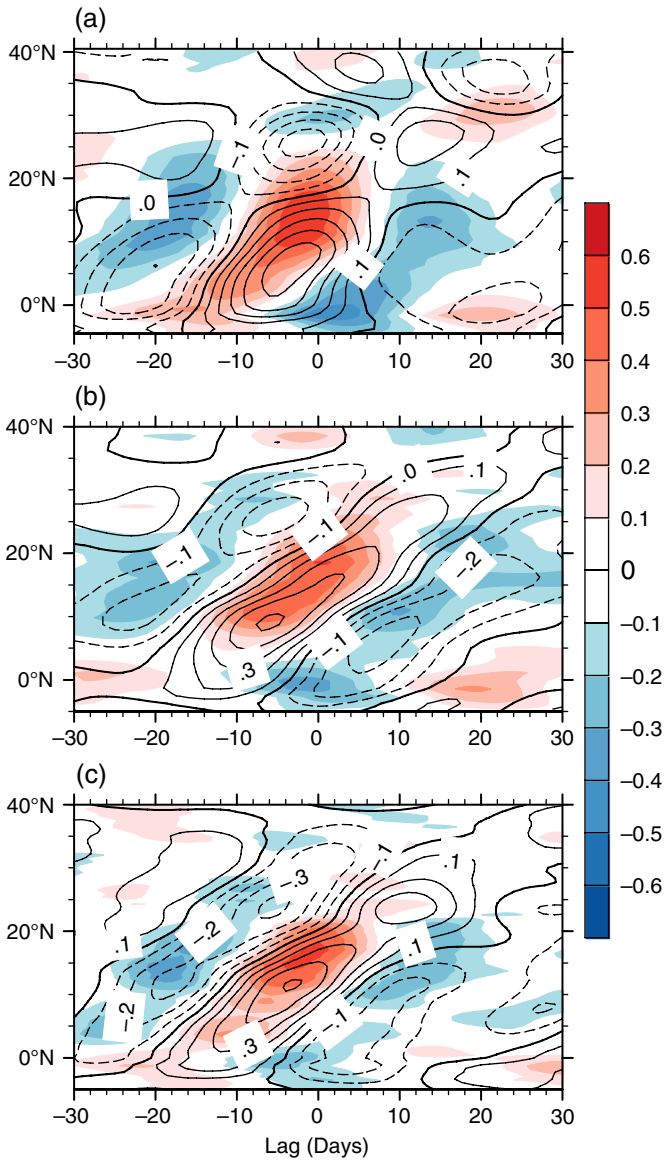

Figure 6. Lag correlation of the 20–70-day filtered precipitation (shaded, mm day^{-1}) and U850 (contour at 0.1 intervals) along 125–135°E upon the filtered precipitation averaged over the SCS and Philippine Sea region (110–130°E, 10–22°N) during 1997–2011 for (a) GPCP and JRA-25 reanalysis, (b) N96, and (c) N216.

develops to the north of this convection. However, there are some differences as well. The precipitation anomaly at N96 simulation is stronger to the north of 20°N and weaker to the south of 10°N (Figure 6(b)), while it is more realistic at N216 (Figure 6(c)).

Figure 7 shows space–time evolution of regressed OLR and 850 hPa wind anomalies with a period of 40–45 days from observation (left column), N96 (middle column) and N216 (right column). It is found that both the N96 (Figure 7(b)) and N216 (Figure 7(c)) capture the observed features of 850 hPa wind and convection anomalies for the BSISO life cycle with a coupled circulation–convection system that propagates northward and northwestward from the equatorial western Pacific. A well-organized anomalous cyclone (anticyclone) in conjunction with the peak enhanced (suppressed) convection alternately dominates the SCS and WNP, forming a dipole pattern. This coupled circulation–convection system is similar to that identified by Hsu and Weng (2001) and Mao *et al.* (2010), indicating a Rossby wave-like behaviour. However, the circulation and convection anomalies at N96 show a slightly northeast–southwestward tilt, while those in the observation and N216 seem to be more zonal. Note that the magnitude of OLR anomaly is improved when increasing resolution, especially for the active (lag day 0) and break phase (lag day −21) of the WNP rainfall (Figures 7(b) and (c)).

3.4. *Structure of the BSISO-related anomalies*

Figure 8 shows the vertical structure of the ISO signal including regressed vorticity, specific humidity and equivalent potential temperature averaged over 125–135°E at lag day +7. It is found that the latitude of the maximum convection centre (MCC) at lag day +7 is about 17°N (Figures 8(j)–(l)) in observation and both two simulations with an improvement in magnitude at N216. In observation, the vertical distribution of vorticity shows (Figure 8(a)) an equivalent barotropic structure and the centres of positive vorticity lie about 2–8° north of the MCC. Maximum specific humidity occurs in the lower troposphere with a centre located over 700 hPa to the north of the MCC (Figure 8(d)) and it contributes to the enhancement of the convective instability by enhancing the equivalent potential temperature (Figure 8(g)). The asymmetric structure of these dynamical and thermodynamical parameters with respect to the MCC, which is found to be key to the northward propagation of the BSISO (Jiang *et al.*, 2004), is well captured in both simulations with similar phase relationship (Figures 8(b), (c), (e), (f), (h), (i)). However, the magnitude of specific humidity and equivalent potential temperature at N96 is obviously stronger than that in observation and N216 simulation (Figures 8(e), (f), (h), (i)). This discrepancy in conjunction with a stronger magnitude of the MCC (Figure 8(k)) may explain the strong BSISO signal (Figure 6(b)) over the East Asia region at N96.

It is well known that the sub-seasonal migrations of the rain band over the East Asia and WNP region are strongly influenced by the intraseasonal variations of the WNPSH and subtropical westerly jet through the modulation of the southwesterly monsoon and upper-level atmospheric divergence (Ding and Chan, 2005; Mao and Wu, 2006; Zhou *et al.*, 2009). Here, composite technique is used to examine the intraseasonal variability of the WNPSH and the subtropical westerly to gain insight into the deficiencies of the model physics. Based on the domain-averaged rainfall anomaly over the SCS and Philippine Sea (10–22°N, 110–130°E), a strong BSISO cycle is defined as one including both an active and a break period, with the peak amplitude of each period greater than a threshold of one standard deviation of the referenced time series. Time-lagged composition is constructed using datasets from 25 days prior to 25 days after, and then averaged over each lead and lag and ensemble over 15 years. Using the above criteria, 36 events are selected for the observation, 27 for N96, and 31 for N216, respectively.

Figure 9 shows the composited unfiltered and filtered 500 hPa geopotential height at time lag of 0 and −21 days, which are the active and break phases of the WNP summer rainfall for both the observation and two simulations. The observed ISOs are characterized by a north–south dipole structure in anomalous geopotential height, corresponding to the westward extension and eastward retreat of the WNPSH as clearly identified from the unfiltered field (Figures 9(a) and (b)). These features are well reproduced at both N96 (Figures 9(c) and (d)) and N216 (Figures 9(e) and (f)), but the geopotential height anomaly to the north of 40°N is not realistically simulated. Note that the simulated unfiltered state of the WNPSH is obviously underestimated for both lag times. The analysis at other lag times (figure not shown) also shows an underestimation of the WNPSH, indicating a systematic model error, which is also found in previous studies (Boo *et al.*, 2010; Bush *et al.*, 2015; MacLachlan *et al.*, 2015). Compared with N96 (Figures 9(c) and (d)), the magnitude of geopotential height anomaly over the WNP is obviously reduced (Figures 9(e) and (f)), which is in better agreement with the observation. Increasing resolution also improves the simulation of unfiltered 500 hPa geopotential height at lag day 0 (Figures 9(c) vs. 9(e)).

Figure 10 shows the composite unfiltered (contour) and filtered (shaded) 200 hPa zonal winds for the observation and the two simulations at time lag of 0 and −21 days. The intraseasonal change of the observed 200 hPa zonal wind manifests in the weak (strong) and slightly southward (northward) extension of the subtropical westerly jet over the East Asia region during the active

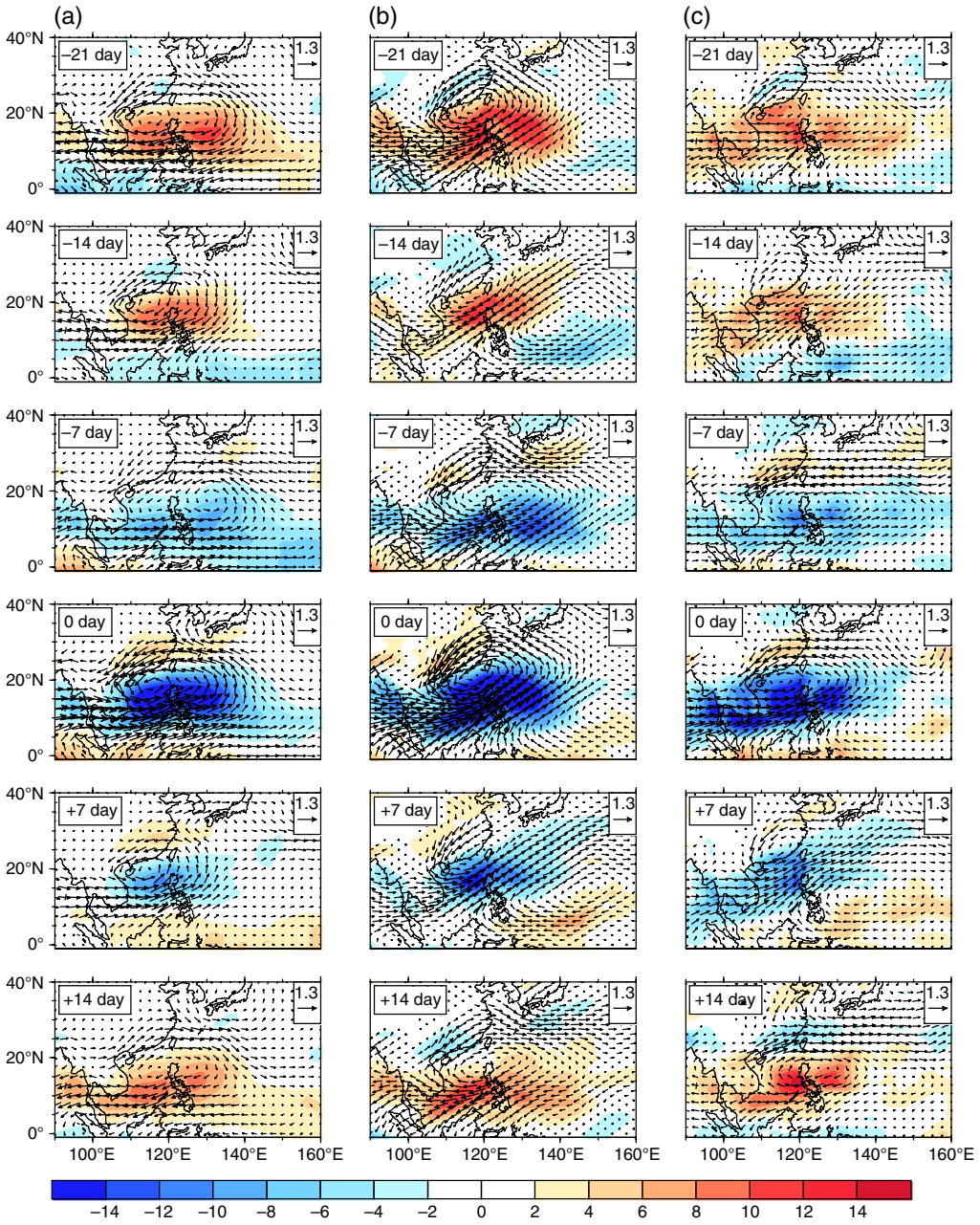

Figure 7. The regressed space–time evolutions of 20–70-day filtered OLR (W m^{-2}, shaded) and 850 hPa wind vectors over the East Asia and WNP region with respect to the rainfall time series averaged in the SCS and Philippine Sea (10–22°N, 110–130°E) for (a, left) JRA-25 and NOAA reanalysis, (b, middle) N96, and (c, right) N216. The regression coefficients have been scaled by one standard deviation of the rainfall time series.

(break) phase of the WNP rainfall (Figures 10(a) and (b)), as illustrated by both the unfiltered and filtered 200 hPa zonal wind. In high summer, the variability of the jet latitude and intensity, on time-scales from synoptic to interannual, in this region is larger than further upstream or during the rest of the year (Schiemann *et al.*, 2009). We show here that some of this variability is explained by the BSISO. Although these intraseasonal changes of 200 hPa zonal wind over the Asian continental region are not well simulated when resolution increases, the change is improved in terms of the position and magnitude for both the filtered and unfiltered field over the North Pacific (Figures 10(c)–(f)), where the sub-seasonal variations of westerly jet are found to be more related to the BSISO rainfall over the EASM and WNP region (Ding and Chan, 2005; Niranjankumar *et al.*, 2011).

3.5. Possible causes for the improvement in BSISO simulation with increasing resolution

To further reveal the reason for the improvement in the simulation of the spatial and temporal variation of the BSISO over the East Asia and WNP region as resolution increases, we first check the difference between N216 and N96 for composited unfiltered near-surface temperature and 500 to 200 hPa averaged temperature over the Asian region at lag day 0 as shown in Figure 11(a). It is found that increasing resolution reduces the near-surface temperature over most of the Asian continent, while the changes are negligible over the ocean region due to the prescribed sea-surface temperature. The 500 to 200 hPa averaged temperature is also reduced to the north of 20°N with the centre located over northeast Asia as resolution increases (Figure 11(a)). Since N96 shows warm biases over most of the East Asian region and especially the Asian continent as shown in Figure 11(b), this change of temperature indicates an improvement in the higher resolution model. Further analysis of the time–latitude section of unfiltered near-surface temperature and 500 to 200 hPa averaged temperature along 95–120°E (Figures 11(c) and (d)) also suggests a reduction of continental temperatures in the higher resolution model, implying reduced land–sea thermal contrast over the East Asia region as resolution increases. Given the fact that the EASM is a result of land–sea thermal contrast (Guo, 1983; Zhu *et al.*, 2005), the change in land–sea thermal contrast indicates a weakened EASM in the higher resolution model.

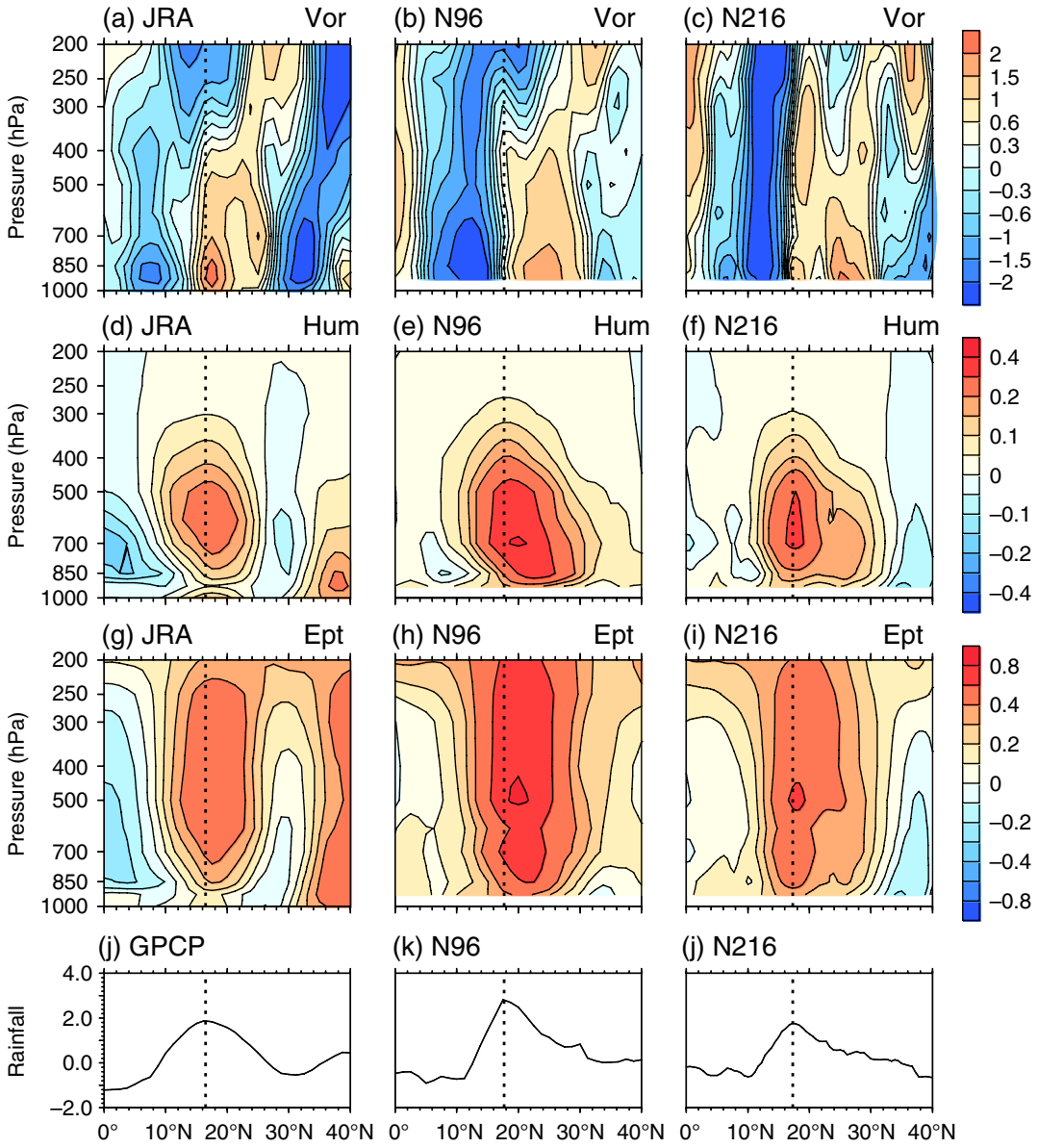

Figure 8. Meridional–vertical structure of (a)–(c) regressed vorticity (10^{-6} s^{-1}), (d)–(f) specific humidity (kg kg^{-1}), (g)–(i) equivalent potential temperature (K), and (j)–(l) amplitudes of rainfall anomalies (mm day^{-1}) at lag day +7 from (a,d,g,j) GPCP and JRA-25 reanalysis, (b,e,h,k) N96, and (c,f,i,l) N216. All variables are averaged over 125–135°E.

Figure 12 shows the composite of the unfiltered precipitation and 850 hPa water vapour transport from the observation, N96 and N216, and the corresponding difference between the N216 and N96 at lag day 0. It is found that the monsoon trough is located over the SCS and Philippine Sea during the active phase of WNP rainfall (Figures 12(a)–(c)). An anomalous anticyclonic moisture transport corresponding to the weakening of the EASM is seen in N216 located over the north SCS and WNP, resulting in precipitation decrease in these regions at higher resolution (Figure 12(d)), while during break phase of the WNP rainfall (at lag day −21), since a strong WNPSH dominates the WNP and SCS region in observation and the two simulations (Figures 9(b), (d), (f)), the difference between N216 and N96 is negligible (figure not shown). These changes of circulation and convection as resolution increases indicate a weakened amplitude of intraseasonal variability, which is more consistent with the observation. On the other hand, the reduction of temperature over the middle and upper troposphere indicates an enhanced meridional temperature gradient over the East Asia region in the higher resolution model. Based on the principle of thermal wind, the subtropical westerly jet is, therefore, stronger and shifted southward as the model resolution increases (Figures 10(e) and (f)). These changes are consistent with many previous studies (Zhou *et al.*, 2009; Li *et al.*, 2010), which showed that the weakening of EASM is characterized by the weakening of the 850 hPa southwesterly winds (Figure 12(d)), a strong WNPSH (Figure 9(e)), strengthened and southward shift of the 200 hPa jet stream (Figures 10(e) and (f)), and a cooling trend in the middle and upper troposphere (Figures 11(a) and (c)).

4. Summary and discussion

The ISO is a prominent feature of the East Asia and WNP summer monsoon. Monsoon prediction on medium-range to seasonal time-scales by dynamical models is strongly dependent on their ability to simulate the BSISO. In this study, we have examined the ability of MetUM GA3.0 with two different horizontal resolutions to simulate the space–time evolution of the BSISO over the East Asia and WNP region from a series of AMIP-style integrations forced by observed daily high-resolution sea-surface temperatures and sea ice. The effect of the model resolution on the model performance and the associated underlying physical mechanisms are further explored and discussed. The main results can be summarized as follows.

The model at two different resolutions can reasonably simulate salient spatio-temporal features of observed BSISO over the East Asia and WNP region in terms of period, dominant REOF mode, variance, northward propagation, cycle evolution and vertical

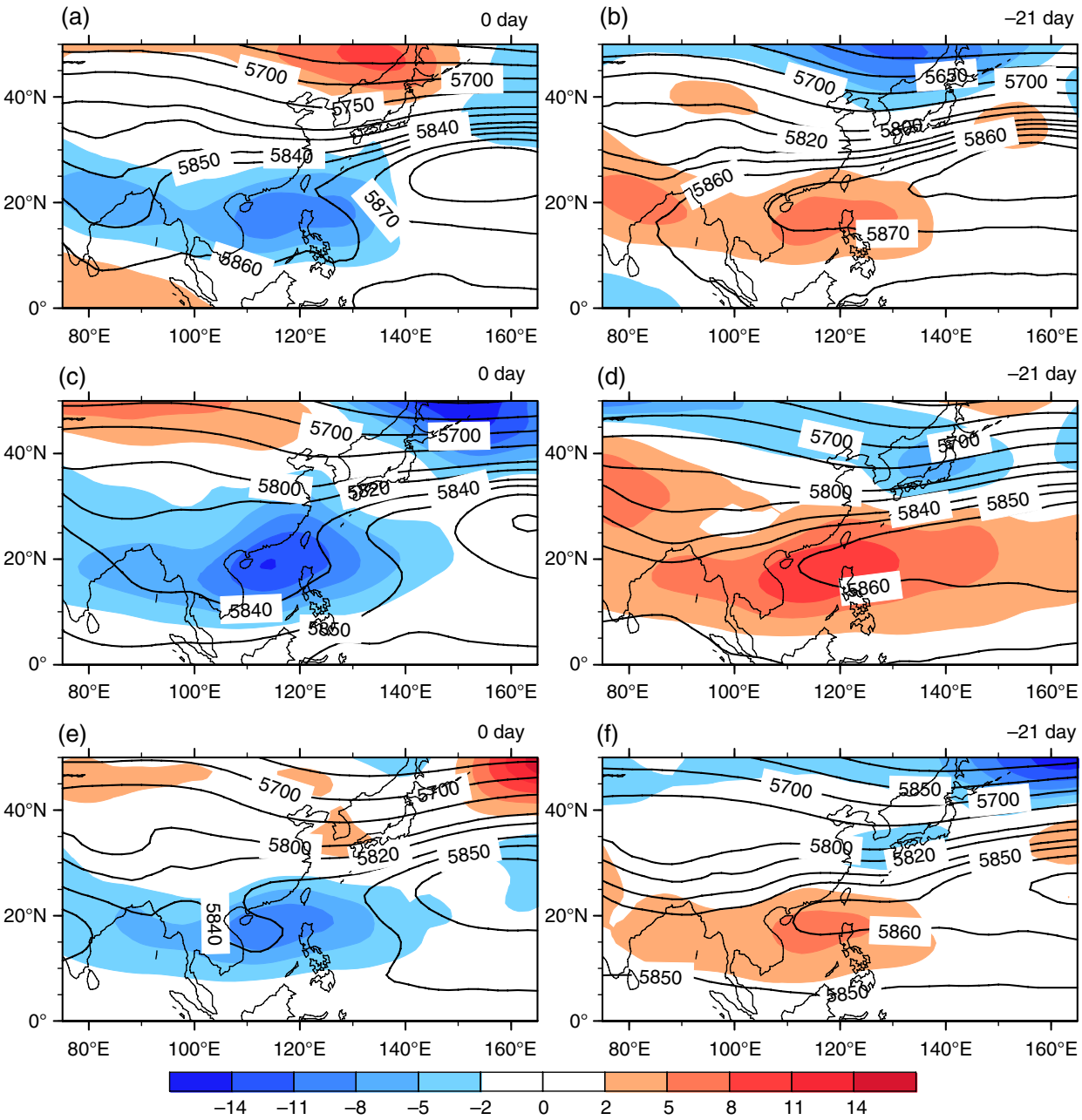

Figure 9. Composites of 20–70-day filtered (shading) and unfiltered (contour) 500 hPa geopotential height (gpm) over the East Asia and WNP region at lag day 0 (left) and −21 (right) from (a,b) JRA-25 reanalysis, (c,d) N96, and (e,f) N216.

structure. The intraseasonal change in intensity and position of the western North Pacific subtropical high and upper troposphere westerly jet associated with the northward propagating BSISOs are also well captured in the model, although the background states of both the WNPSH and upper troposphere westerly jet are weak in the model simulations. The main biases are the overestimation of the BSISO variance of OLR over the whole WNP region and weak northward propagating ISO precipitation signals over the equatorial western Pacific. These biases likely result, at least partially, from the erroneous representation of seasonal mean convection over the equatorial western Pacific region. This result suggests that further improvement in the cumulus and cloud parametrizations, especially for the WNP region, is required.

Although there is little sensitivity of the seasonal mean of the East Asia and WNP summer monsoon to the model horizontal resolution, increasing model resolution leads to an improvement in representing aspects of BSISO. The N96 overestimates the BSISO variance with dominant period longer than the observation, while those at N216 are more realistic. The northward propagating intraseasonal precipitation signals and the REOF structure of BSISO are better simulated at N216 than at N96.The simulation of ISO-related circulation systems is also improved as resolution increases, especially in representing the alternating development of low-level cyclonic and anticyclonic anomalies over the WNP region and the associated zonal change of the WNPSH. Further analysis indicates that these improvements are related to the weakening of background states of the EASM, which is found to be due to the improved simulation of the land–sea thermal contrast as resolution increases.

Demory *et al.* (2014) found that, in several versions of the MetUM, global precipitation shifts from sea to land as resolution increases. The recent study by Johnson *et al.* (2016), also using the GA3.0 UPSCALE integrations, shows a similar result. They concluded that better resolution of orography in the Tropics results in more tropics-wide convergence, and consequently leads to a precipitation increase over land and decrease over the ocean, especially in the equatorial Pacific. This result is consistent with many other resolution sensitivity studies (Liu *et al.*, 2008; Kan *et al.*, 2015), which showed that increasing model horizontal resolution may allow more cloud processes to be resolved by the microphysics scheme rather than by the convection scheme and result in less convective precipitation. The weakening of the emission of Rossby waves (Chen and Murakami, 1988; Mao *et al.*,

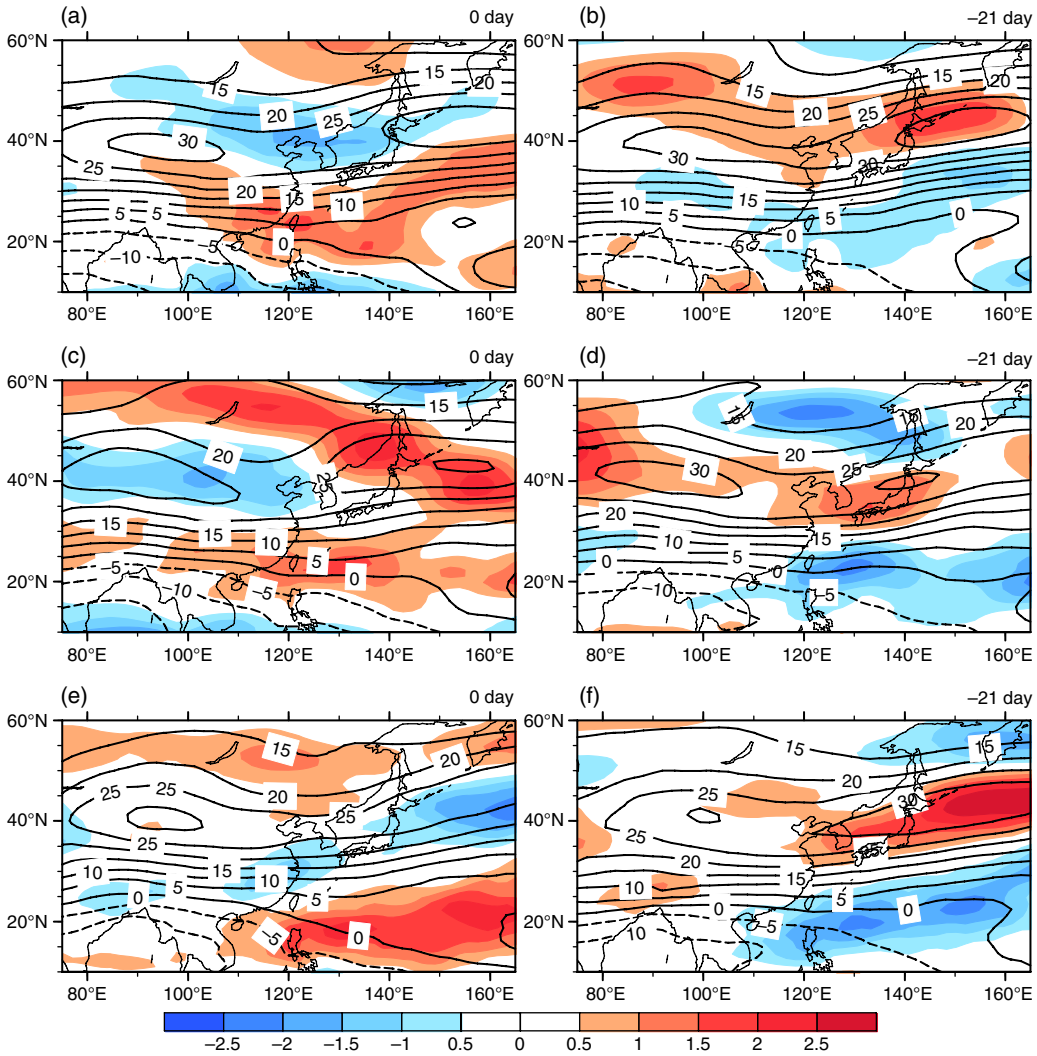

Figure 10. Composites of 20–70-day filtered (shading) and unfiltered (contour) 200 hPa zonal wind ($m\,s^{-1}$) over the East Asia and WNP region at lag day 0 (left) and −21 (right) from (a,b) JRA-25 reanalysis, (c,d) N96, and (e,f) N216.

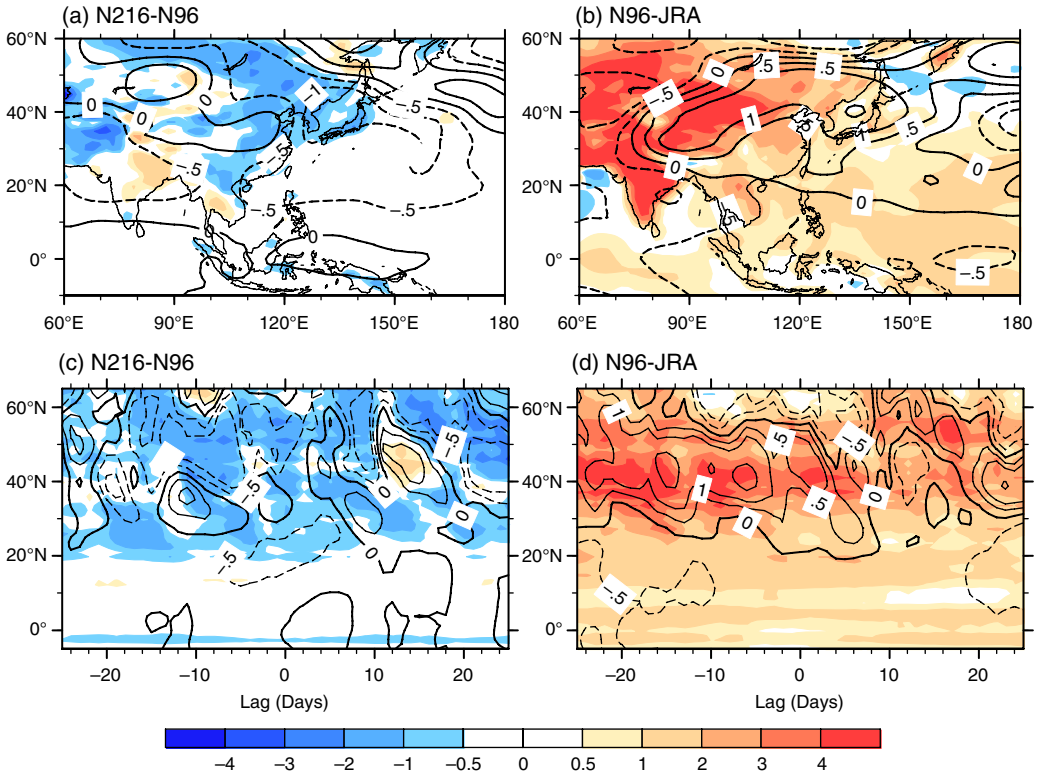

Figure 11. Difference between N216 and N96 for composite of unfiltered surface temperature (shaded, K) and temperature (contour, K) averaged over 500 to 200 hPa for (a) spatial pattern over the Asian region at lag day 0, and (c) the time–latitude section with variables averaged over 95–120°E. (b,d) Same as (a,c), but for the difference between N96 and JRA-25 reanalysis. Contour interval is 0.5 K.

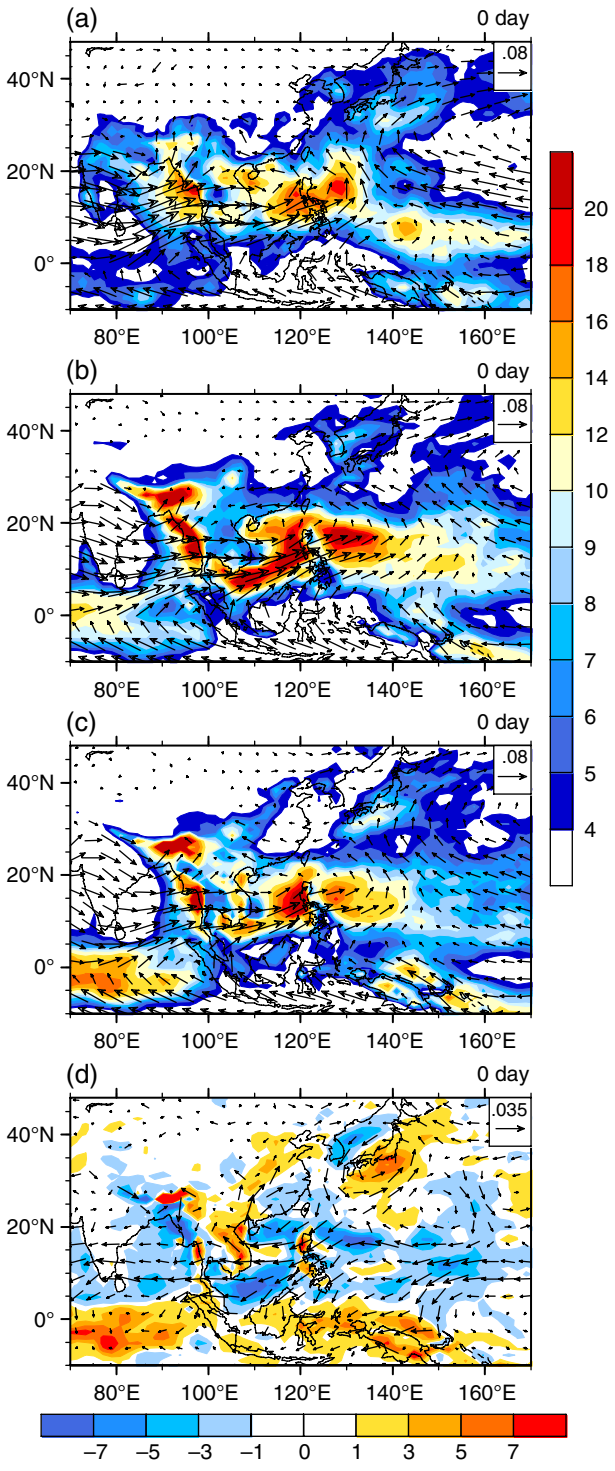

Figure 12. Composites of 20–70-day unfiltered precipitation (shading, mm day^{-1}) and 850 hPa water vapour transport (contour, kg m^{-1} s^{-1}) over the East Asia and WNP region at lag day 0 from (a) GPCP and JRA-25 reanalysis, (b) N96, (c) N216, and (d) the corresponding difference between N216 and N96.

2010), resulting from the convective heating over the equatorial western Pacific, may be responsible for the EASM weakening and the resulting improvement in BSISO simulation in our study. This needs to be explored further through numerical experiments.

Finally, although BSISO simulations made by the higher resolution model were more realistic, difficulty remains in realistic representation of the variance and propagation characteristics of the BSISO for both models. This signifies that change in resolution alone is not sufficient to improve the convectively coupled BSISO variability in the model until convection is explicitly resolved. From this point, updating the cloud and radiation processes and cumulus convection parametrization, which are closely related to the convection and associated BSISO simulation, may be an important step for the future development of the MetUM. Moreover, previous studies suggested that the inclusion of air–sea coupling can lead to significant improvements in BSISO simulations and predictions in terms of the large-scale organization, amplitude and propagation (Fu and Wang, 2004; Seo *et al.*, 2007). Thus, future work will further explore the resolution sensitivity of the East Asian and WNP summer monsoon and its intraseasonal variability in the MetUM coupled model simulations.

Acknowledgements

This work was supported the National Natural Science Foundation of China (Grant No. 41105069 and 41675090) and the National Key Research and Development Program of China (Grant No. 2016YFA0602103). Met Office staff were supported by the Joint UK DECC/DEFRA Met Office Hadley Centre Climate Programme (GA01101) and the UK-China Research & Innovation Partnership Fund through the Met Office Climate Science for Service Partnership (CSSP) China as part of the Newton Fund. The UPSCALE PI was P. L. Vidale (National Centre for Atmospheric Science Climate, NCAS-Climate, Contract R8/H12/83/001 for the High Resolution Climate Modelling (HRCM) programme). We wish to acknowledge PRACE for the grant of supercomputing time and HLRS for supporting us throughout operations on the HERMIT Cray XE6. We acknowledge the significant storage resources and analysis facilities made available to us on JASMIN by STFC CEDA along with the corresponding support teams. We acknowledge use of the MONSooN system, a collaborative facility supplied under the Joint Weather and Climate Research Programme, which is a strategic partnership between the Met Office and the Natural Environment Research Council, and HECToR, the UK Natural Environment Research Council (NERC) and NCAS.

References

Abel SJ, Shipway BJ. 2007. A comparison of cloud resolving model simulations of trade wind cumulus with aircraft observations taken during RICO. *Q. J. R. Meteorol. Soc.* **133**: 781–794, doi: 10.1002/qj.55.

Abhik S, Mukhopadhyay P, Krishna RPM, Salunke KD, Dhakate AR, Rao SA. 2016. Diagnosis of boreal summer intraseasonal oscillation in high resolution NCEP climate forecast system. *Clim. Dyn.* **46**: 3287–3303, doi: 10.1007/s00382-015-2769-9.

Adler RF, Huffman GJ, Chang A, Ferraro R, Xie PP, Janowiak J, Rudolf B, Schneider U, Curtis S, Bolvin D, Gruber A, Susskind J, Arkin P, Nelkin E. 2003. The version-2 Global Precipitation Climatology Project (GPCP) monthly precipitation analysis (1979–present). *J. Hydrometeorol.* **4**: 1147–1167.

Ajayamohan RS, Goswami BN. 2007. Dependence of simulation of boreal summer tropical intraseasonal oscillations on the simulation of seasonal mean. *J. Atmos. Sci.* **64**: 460–478, doi: 10.1175/JAS3844.1.

Boo K-O, Martin GM, Sellar A, Senior CA, Byun Y-H. 2010. Evaluating the East Asian monsoon simulation in climate models. *J. Geophys. Res.* **116**: D01109, doi: 10.1029/2010JD014737.

Bush SJ, Andrew GT, Steven JW, Gill M, Nicholas PK. 2015. The effect of increased convective entrainment on Asian monsoon biases in the MetUM general circulation model. *Q. J. R. Meteorol. Soc.* **141**: 311–326, doi: 10.1002/qj.2371.

Chen TC, Murakami M. 1988. The 30–50-day variation of convective activity over the western Pacific Ocean with emphasis on the northwestern region. *Mon. Weather Rev.* **116**: 892–906.

Demory ME, Vidale PL, Berrisford P, Strachan J, Schiemann R, Roberts MJ, Mizielinski MS. 2014. The role of horizontal resolution in simulating drivers of the global hydrological cycle. *Clim. Dyn.* **42**: 2201–2225, doi: 10.1007/s00382-013-1924-4.

Ding Y, Chan JCL. 2005. The East Asian summer monsoon: An overview. *Meteorol. Atmos. Phys.* **89**: 117–142, doi: 10.1007/s00703-005-0125-z.

Donlon CJ, Martin M, Stark JD, Roberts-Jones J, Fiedler E, Wimmer W. 2012. The Operational Sea-surface Temperature and sea Ice Analysis (OSTIA). *Remote Sensing Environ.* **116**: 140–158, doi: 10.1016/j.rse.2010.10.017.

Duchon CE. 1979. Lanczos filtering in one and two dimensions. *J. Appl. Meteorol.* **18**: 1016–1022.

Fang YJ, Zhang YC, Huang AN, Li B. 2013. Seasonal and intraseasonal variations of East Asian summer monsoon precipitation simulated by a regional air-sea coupled model. *Adv. Atmos.Sci.* **30**(2): 315–329, doi: 10.1007/s00376-012-1241-6.

Fu X, Wang B. 2004. The boreal-summer intraseasonal oscillations simulated in a hybrid coupled atmosphere–ocean model. *Mon. Weather Rev.* **132**: 2628–2649.

Guo QY. 1983. The summer monsoon intensity index in East Asia and its variation. *Acta Geogr. Sin.* **38**: 207–217 (In Chinese).

HadGEM2 Development Team. 2011. The HadGEM2 family of Met Office Unified Model climate configurations. *Geosci. Model Dev.* **4**: 723–757, doi: 10.5194/gmd-4-723-2011.

Hsu HH, Weng CH. 2001. Northwestward propagation of the intraseasonal oscillation in the western North Pacific during the boreal summer: Structure and mechanism. *J. Clim.* **14**: 3834–3850.

Hu WT, Duan AM, Wu GX. 2013. Performance of FGOALS-s2 in simulating intraseasonal oscillation over the South Asian monsoon region. *Adv. Atmos. Sci.* **30**: 607–620, doi: 10.1007/s00376-013-2156-6.

Jiang X, Li T, Wang B. 2004. Structures and mechanisms of the northward-propagating boreal summer intraseasonal oscillation. *J. Clim.* **17**: 1022–1039.

Johnson SJ, Levine RC, Turner AG, Martin GM, Woolnough SJ, Schiemann R, Mizielinski MS, Roberts MJ, Vidale PL, Demory M-E, Strachan J. 2016. The resolution sensitivity of the South Asian monsoon and Indo-Pacific in a global 0.35º AGCM. *Clim. Dyn* **46**: 807–831, doi: 10.1007/s00382-015-2614-1.

Kan M, Huang A, Zhao Y, Zhou Y, Yang B,, Wu H. 2015. Evaluation of the summer precipitation over China simulated by BCC_CSM model with different horizontal resolutions during the recent half century. *J. Geophys. Res. Atmos.* **120**: 4657–4670, doi: 10.1002/2015JD023131.

Kawamura R. 1993. A rotated EOF analysis of global sea surface temperature variability with interannual and interdecadal scales. *J. Phys. Oceanogr.* **24**: 707–715.

Kim DH, Sobel AH, Del Genio AD, Chen YH, Camargo SJ, Yao M-S, Kelley M, Nazarenko L. 2012. The tropical subseasonal variability simulated in the NASA GISS general circulation model. *J. Clim.* **25**: 4641–4659, doi: 10.1175/JCLI-D-11-00447.1.

Lau KM, Chan PH. 1986. Aspects of the 40–50 day oscillation during the northern summer as inferred from outgoing longwave radiation. *Mon. Weather Rev.* **114**: 1354–1367.

Lee SS, Wang B. 2015. Regional boreal summer intraseasonal oscillation over Indian Ocean and western Pacific: Comparison and predictability study. *Clim. Dyn.* **46**: 2213–2229, doi: 10.1007/s00382-015-2698-7.

Li H, Dai A, Zhou T, Lu J. 2010. Responses of East Asian summer monsoon to historical SST and atmospheric forcing during 1950–2000. *Clim. Dyn.* **34**: 501–514, doi: 10.1007/s00382-008-0482-7.

Liebmann B, Smith CA. 1996. Description of a complete (interpolated) outgoing longwave radiation dataset. *Bull. Am. Meteorol. Soc.* **77**: 1275–1277.

Lin H. 2012. Monitoring and predicting the intraseasonal variability of the East Asian–western North Pacific summer monsoon. *Mon. Weather Rev.* **141**: 1124–1138, doi: 10.1175/MWR-D-12-00087.1.

Lin JL, Weichman KM, Kiladis GN, Mapes BE, Schubert SD, Suarez MJ, Bacmeister JT, Lee MI. 2008. Subseasonal variability associated with Asian summer monsoon simulated by 14 IPCC AR4 coupled GCMs. *J. Clim.* **21**: 4541–4567, doi: 10.1175/2008JCLI1816.1.

Liu F, Wang B. 2013. A mechanism for explaining the maximum intraseasonal oscillation center over the western North Pacific. *J. Clim.* **27**: 958–968, doi: 10.1175/JCLI-D-12-00797.1.

Liu P, Kajikawa Y, Wang B, Kitoh A, Yasunari T, Li T, Annamalai H, Fu X, Kikuchi K, Mizuta R, Rajendran K, Waliser DE, Kim D. 2008. Tropical intraseasonal variability in the MRI-20km60L AGCM. *J. Clim.* **22**: 2006–2022, doi: 10.1175/2008JCLI2406.1.

Liu P, Satoh M, Wang B, Fudeyasu H, Nasuno T, Li T, Miura H, Taniguchi H, Masunaga H, Fu X, Annamalai H. 2009. An MJO simulated by the NICAM at 14-km and 7-km resolutions. *Mon. Weather Rev.* **137**: 3254–3268, doi: 10.1175/2009MWR2965.1.

MacLachlan C, Arribas A, Peterson KA, Maidens A, Fereday D, Scaife AA, Gordon M, Vellinga M, Williams A, Comer RE, Camp J, Xavier P, Madec G. 2015. Global Seasonal forecast system version 5 (GloSea5): A high-resolution seasonal forecast system. *Q. J. R. Meteorol. Soc.* **141**: 1072–1084, doi: 10.1002/qj.2396.

Madden RA, Julian PR. 1972. Description of global-scale circulation cells in the Tropics with a 40–50 day period. *J. Atmos. Sci.* **29**: 1109–1123.

Mao JY, Sun Z, Wu GX. 2010. 20–50-day oscillation of summer Yangtze rainfall in response to intraseasonal variations in the subtropical high over the western North Pacific and South China Sea. *Clim. Dyn.* **34**: 747–761, doi: 10.1007/s00382-009-0628-2.

Mao JY, Wu GX. 2006. Intraseasonal variations of the Yangtze rainfall and its related atmospheric circulation features during the 1991 summer. *Clim. Dyn.* **27**:815–830.

Mizielinski MS, Roberts MJ, Vidale PL, Schiemann R, Demory ME, Strachan J, Edwards T, Stephens A, Lawrence BN, Pritchard M, Chiu P, Iwi A, Churchill J, del Cano NC, Kettleborough J, Roseblade W, Selwood P, Foster M, Glover M, Malcolm A. 2014. High resolution global climate modelling; the UPSCALE project, a large simulation campaign. *Geosci. Model Dev.* **7**: 563–591, doi: 10.5194/gmdd-7-563-2014.

Niranjankumar K, Ramkumar TK, Krishnaiah M. 2011. Vertical and lateral propagation characteristics of intraseasonal oscillation from the tropical lower troposphere to upper mesosphere. *J. Geophys. Res.* **116**: D21112, doi: 10.1029/2010JD015283.

Onogi K, Tsutsui J, Koide H, Sakamoto M, Kobayashi S, Hatsushika H, Matsumoto T, Yamazaki N, Kamahori H, Takahashi K, Kadokura S, Wada K, Kato K, Oyama R, Ose T, Mannoji N, Taira R. 2007. The JRA-25 Reanalysis. *J. Meteorol. Soc. Jpn.* **85**: 369–432.

Oouchi K, Noda AT, Satoh M, Wang B, Xie SP, Takahashi H, Yasunari T. 2009. Asian summer monsoon simulated by a global cloud-system resolving model: Diurnal to intra-seasonal variability. *Geophys. Res. Lett.* **36**: L11815, doi: 10.1029/2009GL038271.

Rajendran K, Kitoh A, Mizuta R, Sajani S, Nakazawa T. 2008. High-resolution simulation of mean convection and its intraseasonal variability over the Tropics in the MRI/JMA 20-km Mesh AGCM. *J. Clim.* **21**: 3722–3739, doi: 10.1175/2008JCLI1950.1.

Sabeerali CT, Dandi AR, Dhakate A, Salunke K, Mahapatra S, Rao SA. 2013. Simulation of boreal summer intraseasonal oscillations in the latest CMIP5 coupled GCMs. *J. Geophys. Res. Atmos.* **118**: 4401–4420, doi: 10.1002/jgrd.50403.

Satoh M, Oouchi K, Nasuno T, Taniguchi H, Yamada Y, Tomita H, Kodama C, Kinter J, Achuthavarier D, Manganello J, Cash B, Jung T, Palmer T, Wedi N. 2012. The Intra-Seasonal Oscillation and its control of tropical cyclones simulated by high-resolution global atmospheric models. *Clim. Dyn.* **39**: 2185–2206, doi: 10.1007/s00382-011-1235-6.

Schiemann R, Lüthi D, Schär C. 2009. Seasonality and interannual variability of the westerly jet in the Tibetan Plateau region. *J. Clim.* **22**: 2940–2957, doi: 10.1175/2008 JCLI2625.1.

Seo KH, Schemm JKE, Wang W, Kumar A. 2007. The boreal summer intraseasonal oscillation simulated in the NCEP Climate Forecast System: The effect of sea surface temperature. *Mon. Weather Rev.* **135**: 1807–1827, doi: 10.1175/MWR3369.1.

Shukla RP. 2014. The dominant intraseasonal mode of intraseasonal South Asian summer monsoon. *J. Geophys. Res. Atmos.* **119**: 635–651, doi: 10.1002/2013JD020335.

Taylor KE. 2001. Summarizing multiple aspects of model performance in a single diagram. *J. Geophys. Res.* **106**: 7183–7192, doi: 10.1029/2000JD900719.

Waliser DE, Jin K, Kang IS, Stern WF, Schubert SD, Wu MLC, Lau KM, Lee MI, Krishnamurthy V, Kitoh A, Meehl GA, Galin VY, Satyan V, Mandke SK, Wu G, Liu Y, Park CK. 2003. AGCM simulations of intraseasonal variability associated with the Asian summer monsoon. *Clim. Dyn.* **21**: 423–446, doi: 10.1007/s00382-003-0337-1.

Walters DN, Best MJ, Bushell AC, Copsey D, Edwards JM, Falloon PD, Harris CM, Lock AP, Manners JC, Morcrette CJ, Roberts MJ, Stratton RA, Webster S, Wilkinson JM, Willett MR, Boutle IA, Earnshaw PD, Hill PG, MacLachlan C, Martin GM, Moufouma-Okia W, Palmer MD, Petch JC, Rooney GG, Scaife AA, Williams KD. 2011. The Met Office Unified Model Global Atmosphere 3.0/3.1 and JULES Global Land 3.0/3.1 configurations. *Geosci. Model Dev* **4**: 919–941, doi: 10.5194/gmd-4-919-2011.

Wang B, Xie X. 1997. A model for the boreal summer intraseasonal oscillation. *J. Atmos. Sci.* **54**: 72–86.

Wang B, Zhou X. 2008. Climate variation and prediction of rapid intensification in tropical cyclones in the western North Pacific. *Meteorol. Atmos. Phys.* **99**: 1–16, doi: 10.1007/s00703-006- 0238-z.

Wilson DR, Bushell AC, Kerr-Munslow AM, Price JD, Morcrette CJ. 2008. PC2: A prognostic cloud fraction and condensation scheme. I: Scheme description. *Q. J. R. Meteorol. Soc.* **134**: 2093–2107, doi: 10.1002/qj.333.

Wu P. 1993. Nonlinear resonance and instability of planetary waves and low-frequency variability in the atmosphere. *J. Atmos. Sci.* **50**: 3590–3607.

Wu P, Li C. 1990. *The 10–20 Day Oscillation in the Atmosphere*. Special Issue of Collected Papers. Chinese Journal of Atmospheric Sciences. Science Press: Beijing.

Yasunari T. 1979. Cloudiness fluctuations associated with the Northern Hemisphere summer monsoon. *J. Meteorol. Soc. Jpn.* **57**: 227–242.

Zhou TJ, Yu RC, Zhang J, Drange H, Cassou C, Deser C, Hodson DLR, Sanchez-Gomez E, Li J, Keenlyside N, Xin XG, Okumura Y. 2009. Why the western Pacific subtropical high has extended westward since the late 1970s. *J. Clim.* **22**: 2199–2215, doi: 10.1175/2008JCLI2527.1.

Zhu C, Lee WS, Kang H, Park CK. 2005. A proper monsoon index for seasonal and interannual variations of the East Asian monsoon. *Geophys. Res. Lett.* **32**: L02811, doi: 10.1029/2004GL021295.